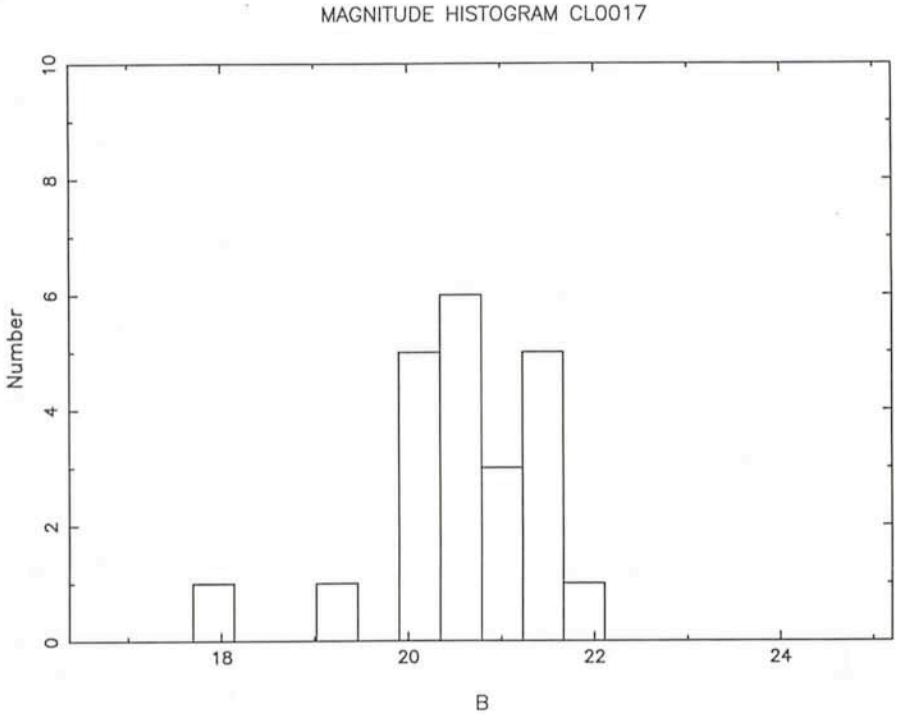

Figure 2: *Histogram of corrected B magnitudes.*

outliers 22 out of 26 galaxies remained. A Kolmogorov-Smirnov test which compares our distribution of velocities to a gaussian distribution returned a significance level larger than 95%. The uncorrected line-of-sight velocity dispersion and mean recession velocity are $\sigma = 1466\ \mathrm{kms}^{-1}$ and $v = 81{,}540\ \mathrm{kms}^{-1}$ respectively.

We then applied the method described in Gourgoulhon et al. (1992) to determine the virial mass and mass-to-light ratio of the cluster. As the collapse time of the cluster (2 Gyr) is small compared to the Hubble time, the cluster is virialized, and its virial mass is a good estimator of its total mass.

We first correct our raw data for various effects: K-corrections are adopted from Pence (1976), and amount to −1.27 and −0.66 in the B and V-bands, respectively; evolutionary corrections are taken from Arimoto and Yoshii (1987) for a 10^{11} $M_\odot$ E/S0 galaxy, and amount to +0.34 and +0.08 for V-magnitudes and (B-V) colours, respectively; relativistic corrections to mass and mass-to-light ratio multiply uncorrected values by 0.42 and 0.35, respectively. The dependence of these corrections upon adopted values of H_o, q_o and z_f (redshift of formation) is small at the cluster redshift (0.272). Due to the location of the cluster (South Galactic Pole), galactic absorption is neglected; internal absorption is neglected as well, because most of our sample galaxies are early-type.

We obtain a corrected mass of 7.0×10^{14} $M_\odot$. For each galaxy, the uncorrected magnitude in the B-band is evaluated from Gunn g and r magnitudes, using Kent's (1985) relations. The corrected B-magnitude is then calculated adding $-1.27+(0.34+0.08) = -0.85$. The mean observed colour is $g-r = 0.90$, corresponding to $B-V = 1.46$. Applying the K-and evolutionary corrections to this value gives a corrected B−V at redshift 0 of 0.93 (typical of E/S0 galaxies), confirming the order of magnitude of these corrections. The total luminosity of the cluster in the B-band is obtained after correction for the contribution of faint members not measured. To make this correction, we integrate a Schechter luminosity function from the limiting magnitude of a complete sub-sample down to infinity. Figure 2 shows that our sample of 22 galaxies is complete down to a corrected B-magnitude of 20.8. Adopting a luminosity distance of 1200 Mpc, the correcting factor for incompleteness is 2.18. As the total luminosity of the galaxies brighter then 20.8 is 3.9×10^{11} $L_\odot$, we adopt a total luminosity of the cluster of $8.5\times10^{11}L_\odot$, corrected for relativistic effects and incompleteness. 20% of this luminosity is concentrated in the nucleus.

Finally, we derive a mass-to-light ratio in the B-band of 820 $M_\odot/L_\odot$.

3. Conclusions

Rich, compact and massive galaxy clusters at redshifts between 0.2 and 0.5 with line of sight velocity dispersions exceeding 700 km/s are good gravitational lens candidates. They distort background galaxies which are as far as twice the cluster distance. The magnification and distortion of these galaxies provide an independent method to detemine cluster masses and to study objects at high redshifts.

CL0017 is one of the best lens candidates available. It possesses a mass of 7.0×10^{14} $M_\odot$ and a luminosity of 8.5×10^{11} $L_\odot$ ($M/L = 820\ M_\odot/L_\odot$), much of it in a very compact nucleus of size $77h^{-1}$ Mpc. Because of its high mass and high M/L ratio, CL0017 becomes an excellent candidate to search for multiple arcs and, therefore, probe the dark matter independently.

References

Arimoto, N., Yoshii, Y. 1987, *A&A*, **173**, 23.

Butcher, H., and Oemler, A. 1984, *Ap. J.*, **285**, 426.

Gourgoulhon, E., Chamaraux, P., Fouqué, P. 1992, *A&A*, **255**, 69.

Infante, L., Giraud, E., and Triay, R. 1991, *The Messenger*, **64**, 65.

Infante, L., Pritchet, C.J., and Quintana, H. 1986, *A.J.*, **91**, 217.

Infante, L., Giraud, E., Quintana, H., Way, M., and Hertling, G. 1992, In preparation.

Kent, S.M. 1985, *P.A.S.P.*, **97**, 165.

Pence, W. 1976, *Ap.J.*, **203**, 39.

Tyson, A. 1992, *Physics Today*, Vol. **45**, No. **6**, 24.

New Features of IRSPEC

R. GREDEL and U. WEILENMANN, ESO La Silla

In January 1991, IRSPEC at the NTT was equipped with a 58×62 pixel InSb array from Santa Barbara Research Center (SBRC). The chip replaced a 1D array and brought new observing features such as long-slit capability. The new system is discussed in the March 1991 issue of *The Messenger* **63,** p. 77. IRSPEC has been further improved in the meanwhile. Recent instrumental modifications have resulted in a higher sensitivity in the 1 – 2.5-μm region. Operational enhancements such as the implementation of automatic beam-switching and continuous mode have increased the efficiency of observations with IRSPEC. The modifications were carried out by Peter Biereichel, Gert

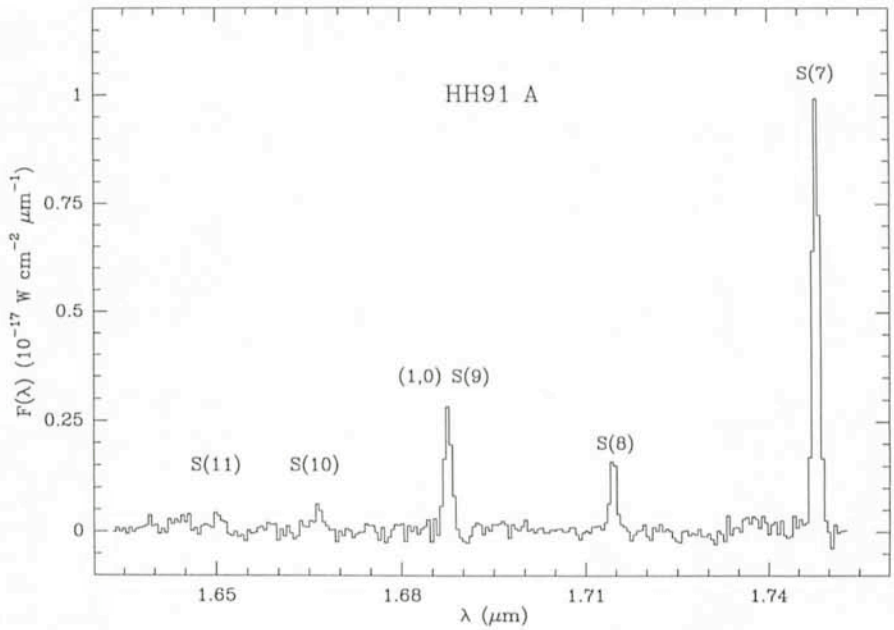

Figure 1: *H-band spectrum of the Herbig-Haro object HH 91A. Monochromatic fluxes in units of 10^{-17} W cm^{-2} μm^{-1} are plotted vs. wavelength λ in μm. Individual rotational transitions that arise in the S-branch of the (1,0) band of H_2 are identified.*

Finger, Manfred Meyer and Jean-Louis Lizon from Garching, and Flavio Gutiérrez and one of the authors (U.W.) from La Silla.

The following contains a discussion of the recent instrumental changes and the new observing modes that are now available. It also summarizes some of the scientific results obtained with IRSPEC during the last year to illustrate the applications of the instrument.

Instrumental Enhancements

In April/May 1991, non-destructive multiple readout was installed as part of the data-acquisition software. In this mode, the output voltages of the pixels are continuously sampled at a rate of 19 s^{-1} without resetting. A linear regression is fit through the individual "readouts", which results in a significant reduction of the effective read-noise. Several measures were taken to suppress the internal background, including screening of the light path and blocking of remaining light leaks in the cold shield. In J, H and K, these measures have reduced the RMS noise to less than 200 e for detector integration times (DITs) of a few tens of seconds. For DITs longer than about a minute, the noise increases due to shot noise. Other hardware modifications included modifications of various components of the opto-mechanical functions, such as the grating exchange mechanism, which caused some trouble in the past. Only one of the previously reported shortcomings remains: about 20 % of the slit remains vignetted by the filters which were not sized for the SBRC array. Given the fact that the usable length of the slit is about 100", however, this drawback does not influence observations with IRSPEC.

New Observing Modes

The software that handles the spectrometer setting was rewritten and transferred from an old HP 1000 to the main HP A900 instrument computer. Spectrometer and instrument parameters are set via form filling or through typed commands. In April 1992, two new observing procedures, *continuous mode* and *beam switching*, were implemented. It is now possible to obtain a full spectrum with specified beginning and end wavelength and the respective sky frames automatically. The pixel overlap between adjacent spectral segments, the number of object-sky pairs per grating setting, and the reference position can be entered as well. The system then performs the given number of integrations per grating setting, offsets the telescope to obtain explicit sky measurements, if desired, and steps the grating successively through the given wavelength range to obtain the full spectrum. The automatic observing procedures not only remove overheads that were introduced in the past when many of these steps had to be performed manually. They also eliminate a source of error and make sure that the observer leaves La Silla with a complete set of measurements, without sky frames missing or gaps in his or her spectra.

In the future, it is expected to increase the wavelength encoder resolution from presently 2.6 encoder steps per pixel by about a factor of 4. Thus, settings to particular wavelengths will become more reproducible. A transfer of IRSPEC data to a SUN workstation is planned to allow on-line data reduction using existing MIDAS routines.

Scientific Results

HH 90/91. Figures 1 and 2 show the H- and K-band spectra obtained to-

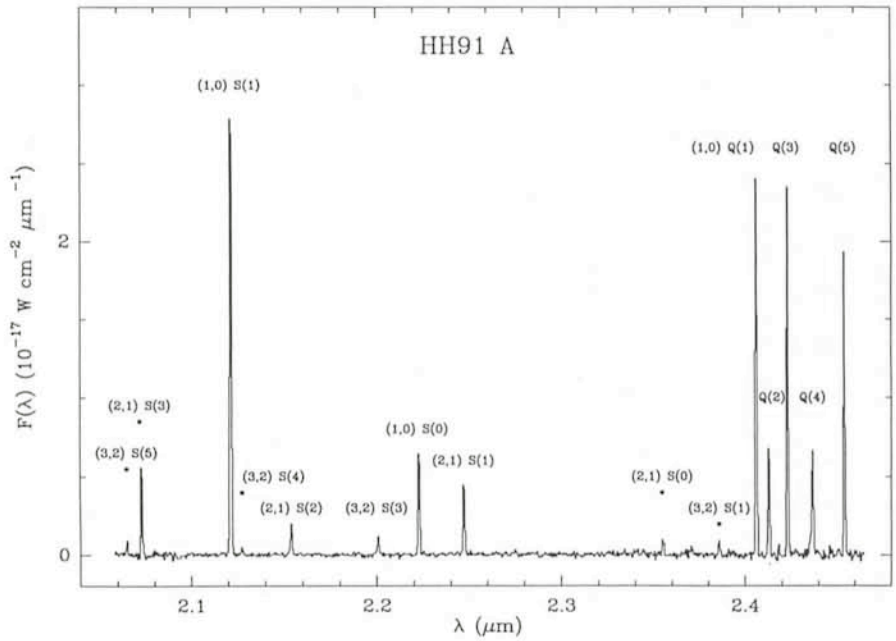

Figure 2: *K-band spectrum of HH 91A. Labels as in Figure 1. The spectrum is a composite of 16 individual segments obtained with an integration time of 8 min each, equally shared between object and sky.*

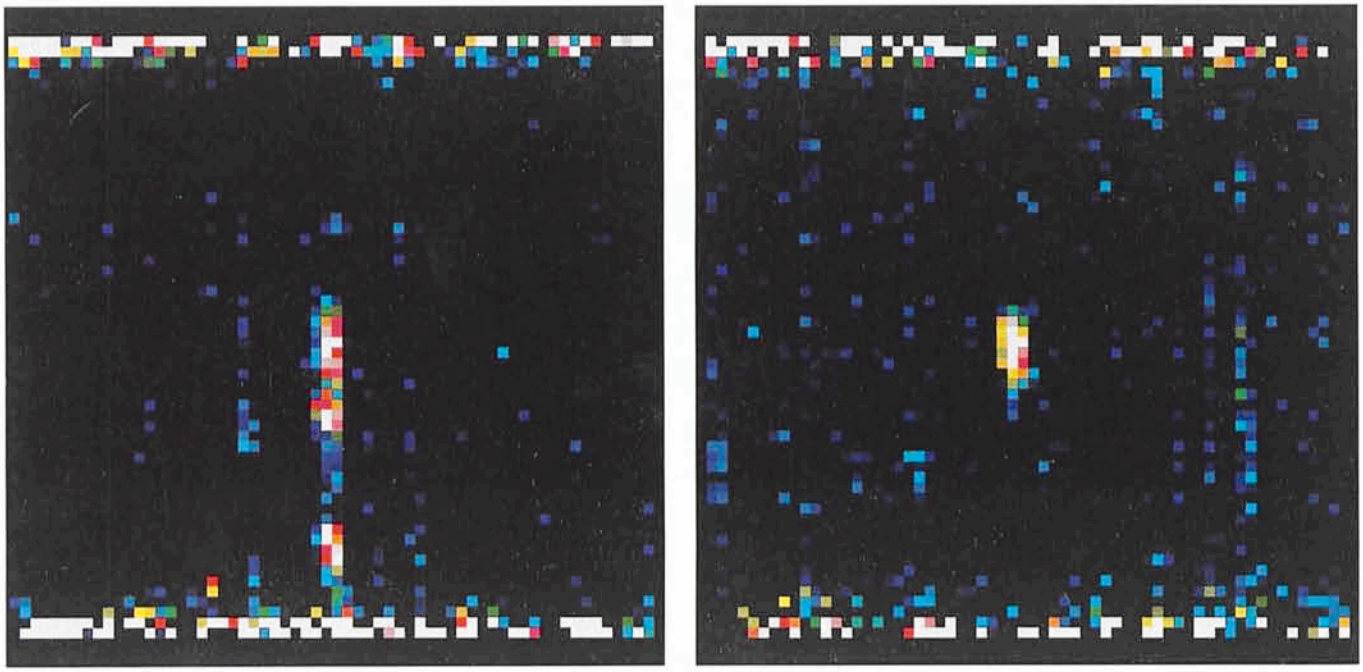

Figure 3: *Sky-subtracted frames of the HH 111 jet in [FeII] 1.644 μm (left panel) and H_2 2.121 μm (right panel). Wavelengths are in X and the slit is in Y direction. The slit is oriented along the jet axis. The on-source integration times are 5×60 s. The white horizontal pattern at the extremes of the slit are introduced by the flat-fielding and mark the region that is vignetted.*

wards the low-excitation Herbig-Haro (HH) object HH 91A. HH 91A is a bright knot in the HH complex HH 90/91 in Orion (Gredel et al. 1992). The spectra are dominated by emission lines of molecular hydrogen that arise from the electric quadrupole cascade in the $X^1\Sigma_g^+$ groundstate of H_2. Individual lines are identified in the spectra. The spectrum shown in Figure 2 consists of 16 individual segments, each obtained with an integration time of 4×1 min on the object and a similar time on a reference position. The resolution is $\lambda/\Delta\lambda$ = 2500. The inferred population densities of the H_2 levels follow a thermal distribution which is characterized by an excitation temperature of 2750 K. It is believed that the emission lines seen in HH objects arise from the recombination region behind a shock. The excitation temperature measured in HH 91A indicate shock velocities of a few tens of km/s. Non-thermal excitations of H_2 levels which can be introduced by UV photons that are expected to arise in the apex of strong bow-shocks are not observed in HH 91A. The reddening towards HH 91A can be determined from a comparison of the intensities in the (1,0) S(1) and the (1,0) Q(3) lines which arise from a common upper level. A value of $E_{B-V} \leq$ 0.6 mag is found.

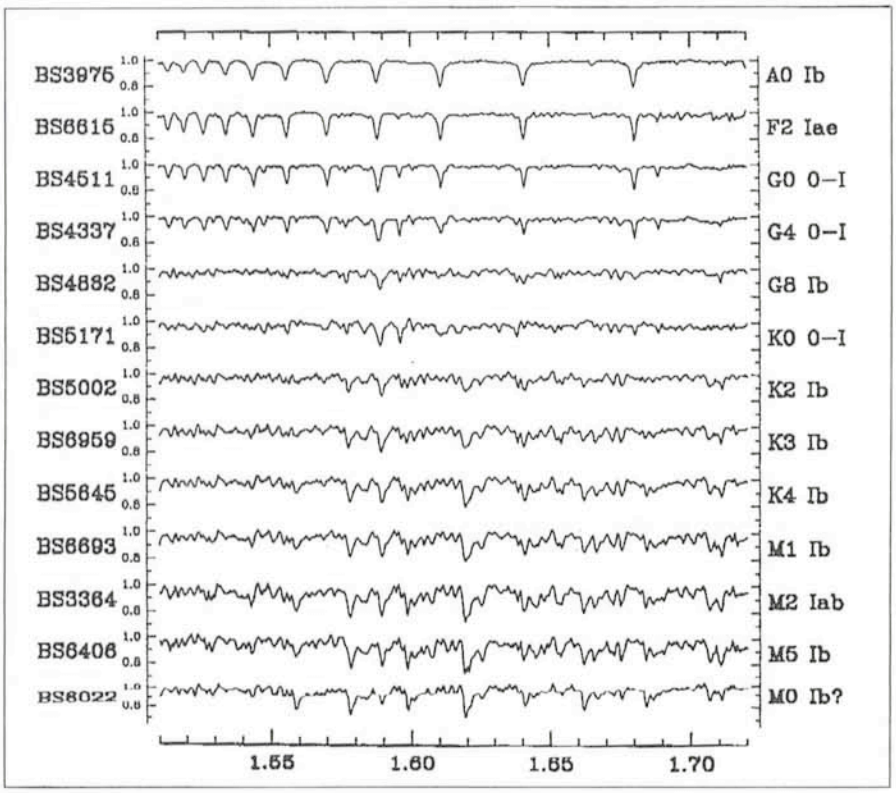

Figure 4: *H band spectra of supergiant stars.*

HH 111. Figure 3 shows two IRSPEC frames in [FeII] (1.644 μm) and H_2 (2.121 μm) obtained towards the well collimated HH jet HH 111. The frames are sky-subtracted and flat-fielded using an internal halogen lamp. A tilt of the spectral lines in the raw frames, introduced by the off-axis Littrow mount of the grating, has been removed by shifting each row appropriately. The enhanced background that can be seen in the upper and lower part in both frames results from the flat-fielding and marks the parts of the slit that are vignetted. The slit is in Y direction and has a scale of 2.2″ per pixel. It is aligned along the HH 111 jet and centred on knot H (see e.g. Reipurth 1991). The H_2 frame shows three emission maxima along the jet and follows the intensity distribution of Hα, as inferred from a CCD frame obtained at the Danish 1.5-m telescope. The three maxima seen in the H_2 frame correspond to knots D-H, knot L, and knot P (Reipurth 1991). [FeII], on the other

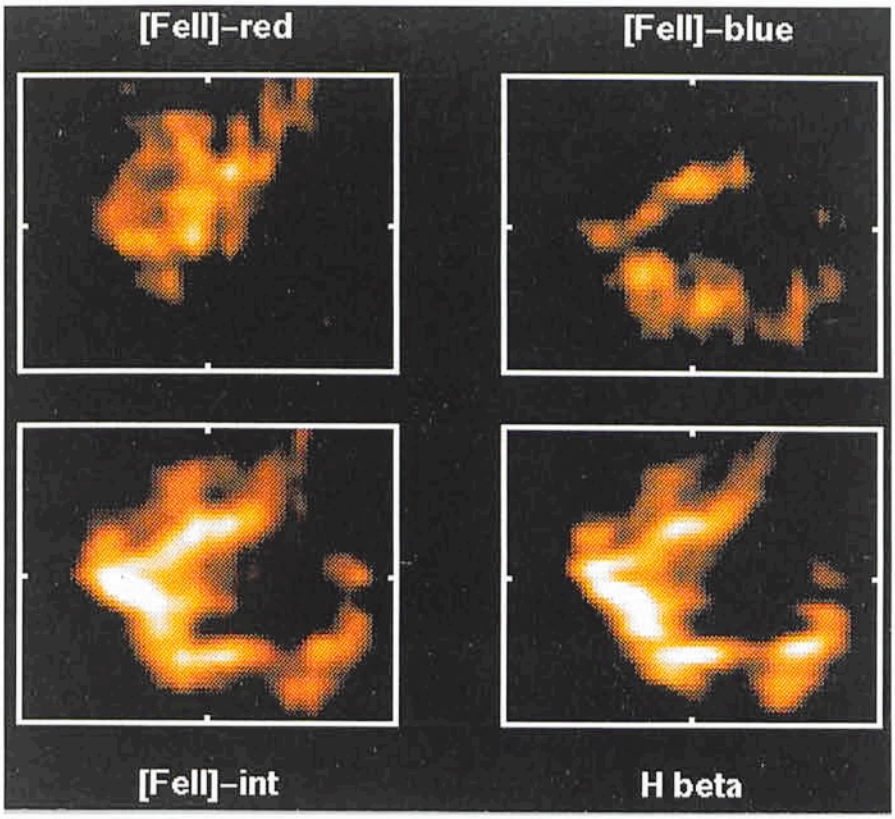

▲

Figure 5: *Images of the LMC supernova remnant N 49 in the [FeII] (1.644 μm) line obtained by slit scanning. The field is approximately 1′ with N at the top and E to the left. The upper panels show images in velocity bands 200 km/s wide. The lower [FeII] image is integrated over all velocities. It has the same cut levels as the Hβ interference frame shown in the lower right.*

side, has a significantly different distribution. In particular, the [FeII] emission is strong near knots D-H, whereas it is weak around knots L and P.

Giants/Supergiants. The high resolution of IRSPEC has initiated a spectral classification programme of giant and supergiant stars (Origlia et al. 1992). Figure 4 shows spectra of A-M supergiant stars between 1.51 μm and 1.72 μm. The spectra of the hottest stars with A-G spectral types are dominated by Brackett series hydrogen absorption lines. The cooler stars show a variety of molecular and atomic absorption bands whose equivalent widths increase towards later spectral types. Note that the reproducibility of the faintest spectral features indicates that the noise in these spectra is comparable to or less than the thickness of the traces.

N 49. IRSPEC can be used to obtain spectral line images of extended objects. An example is shown in Figure 5 which contains [FeII] images of the supernova remnant N 49 in LMC. The images are reconstructed from individual IRSPEC frames, obtained by scanning the slit across the object. The red and blue [FeII] images, shown in the upper part, contain the emission integrated in 200 km/s wide bands, centred 270 km/s to the red and blue of the systemic velocity. They reveal an interesting velocity structure which suggests that the northern and southern filaments are probably located on opposite sides of an expanding shell. In the lower part of Figure 5, the [FeII] image, obtained by integrating over all velocities, is compared to an Hβ interference filter image obtained with the CCD camera at the 2.2-m telescope. The latter frame has been smoothed to the same spatial resolution (≈ 2″) as the IRSPEC image. Both images have the same cut levels, and show that the morphology and the

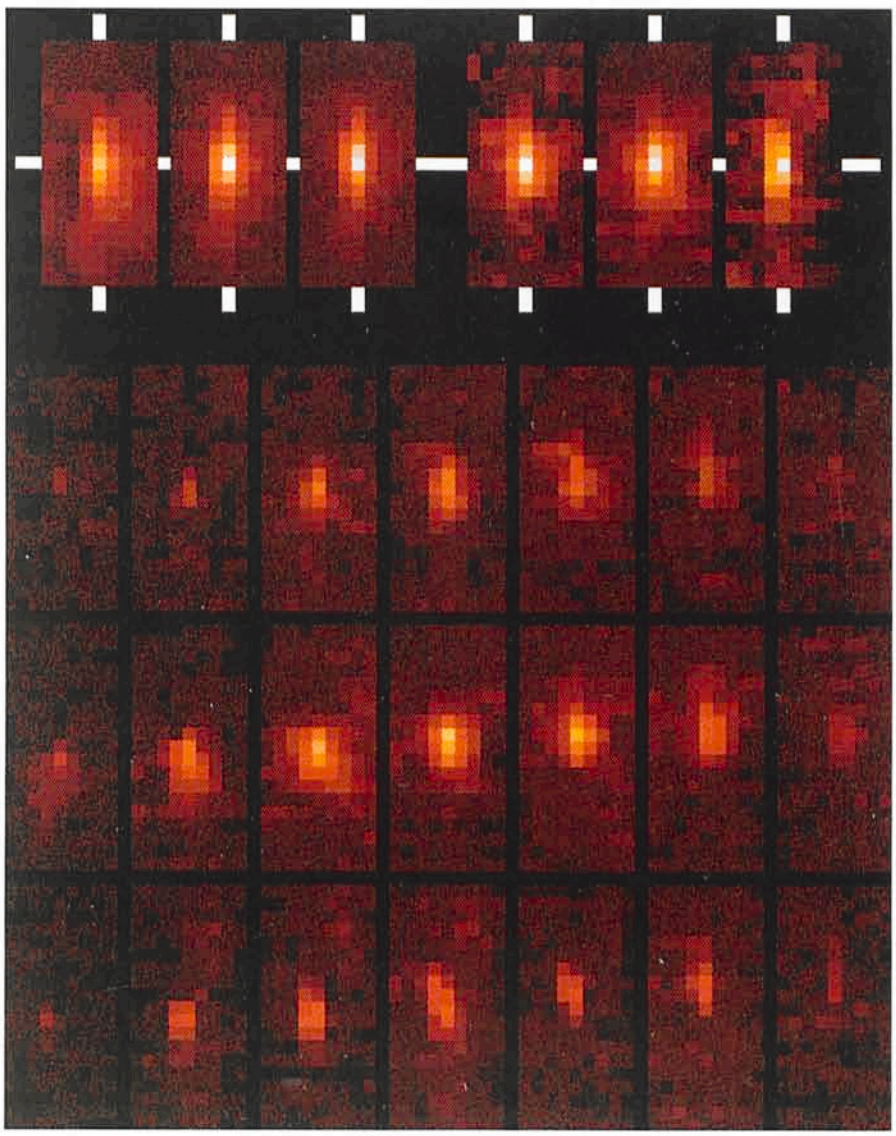

▶

Figure 6: *Images of the nearly edge-on late type spiral galaxy NGC 4945 obtained by stepping the IRSPEC slit. The upper row shows the continuum image (three frames to the left) and the corresponding emission in [Fe II] (1.644 μm), H_2 (2.121 μm) and Brγ (2.167 μm) (three frames to the right). The second, third and fourth rows show seven images in each of these three lines, in steps of 1 pixel, i.e. at increasing velocity, from left to right.*

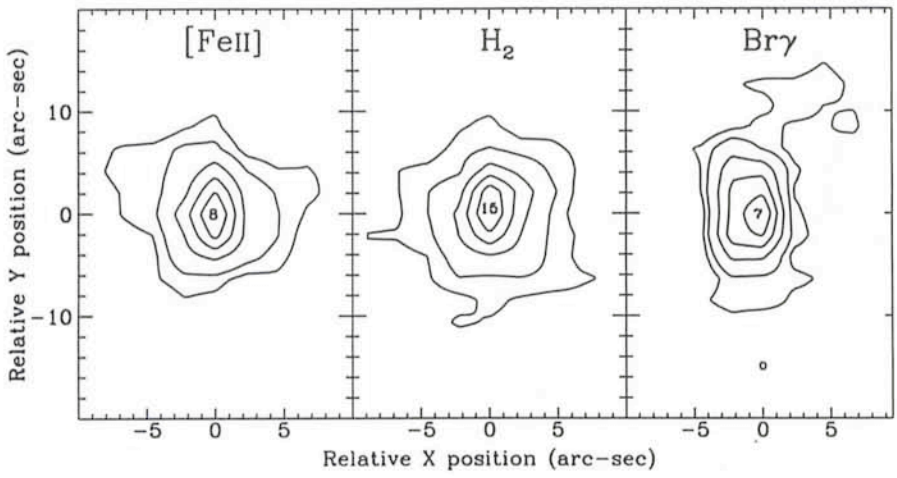

Figure 7: *Contour maps of NGC 4945 in [FeII], H_2, and Brγ.*

surface brightness seen in [FeII] and Hβ are remarkably similar.

NGC 4945. Figure 6 contains images of the nearly edge-on late type spiral NGC 4945, obtained by stepping the IRSPEC slit. The upper six panels show emission in the continuum (left) and [FeII], H_2 and Brackett γ lines (right) at 1.644 μm, 2.121 μm and 2.167 μm, respectively. The lower panels show images in the same lines but in velocity slices separated by 1 pixel or 97 km/s for [FeII] and 66 km/s for the other two lines. The dynamics is dominated by a velocity gradient of 15 km/s/arcsec. This is the same as that obtained from millimetre CO observations which reveal the presence of a molecular disk or torus in which the infrared line emitting region is embedded (Moorwood and Oliva 1992).

Figure 7 contains the contour maps of NGC 4945 in the [FeII], H_2 and Brγ lines. The emission in all three lines extends ≈ 650 pc along the major axis which is parallel to the Y axis in this figure. Of most interest, however, is the similarity of the [FeII] and H_2 distributions and the fact that they are more extended than the Brγ emission along the minor axis. Taking into account also the integrated line luminosities and ratios it appears most likely that the Brγ emission arises in gas photoionized by hot stars in a nuclear starburst while the [FeII] and H_2 lines are shock excited by a supernova driven superwind (Moorwood and Oliva 1992).

NGC 1068. Figure 8 contains complete J, H and K band spectra of the Seyfert galaxy NGC 1068 showing a wide range of identified spectral features and some whose origin is still unclear. More than 50 grating settings were required. The integration time per setting was 60 s. Of particular interest are the strong and broad [SiVI] (1.96 μm) (blended with narrow H_2 (1,0) S(3) emission) and [SiVII] (2.48 μm) coronal lines and the wealth of stellar absorption features in the H band (Moorwood and Oliva 1992).

PKS 0237-23. The high sensitivity of IRSPEC allows the study of quasars in the near infrared. Studies in the UV and optical wavelength region have revealed the presence of different classes of sharp line absorption systems at redshifts lower than that of the quasars. Among those are metal-line systems believed to arise in HII regions in gas-rich and star-forming intervening dwarf galaxies. This hypothesis can be tested by searching for Hα lines at redshifts smaller than that of the quasar, and other unequivocal signatures of an HII

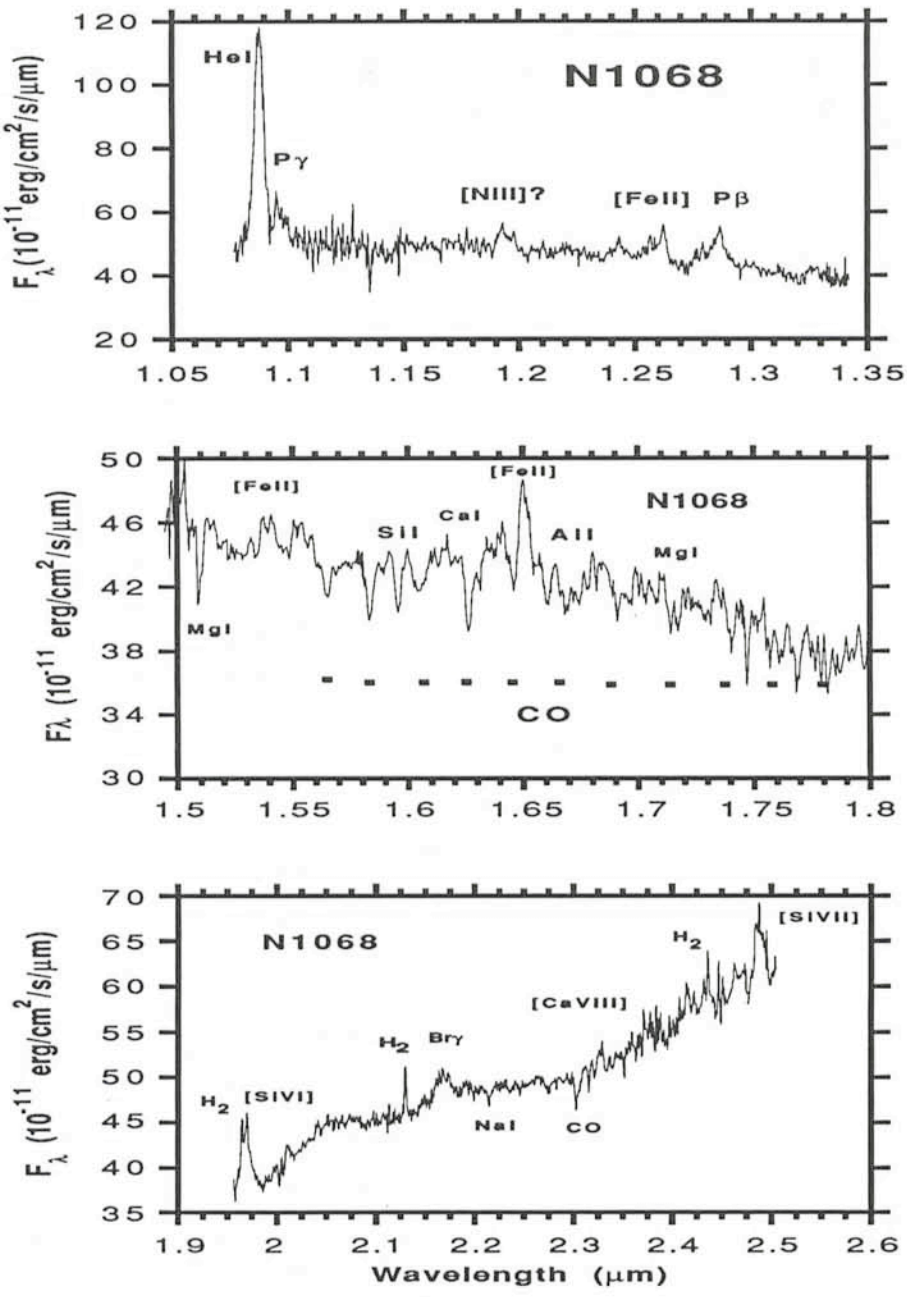

Figure 8: *Complete J, H and K band spectra of the Seyfert galaxy NGC 1068. Individual spectral features are identified.*

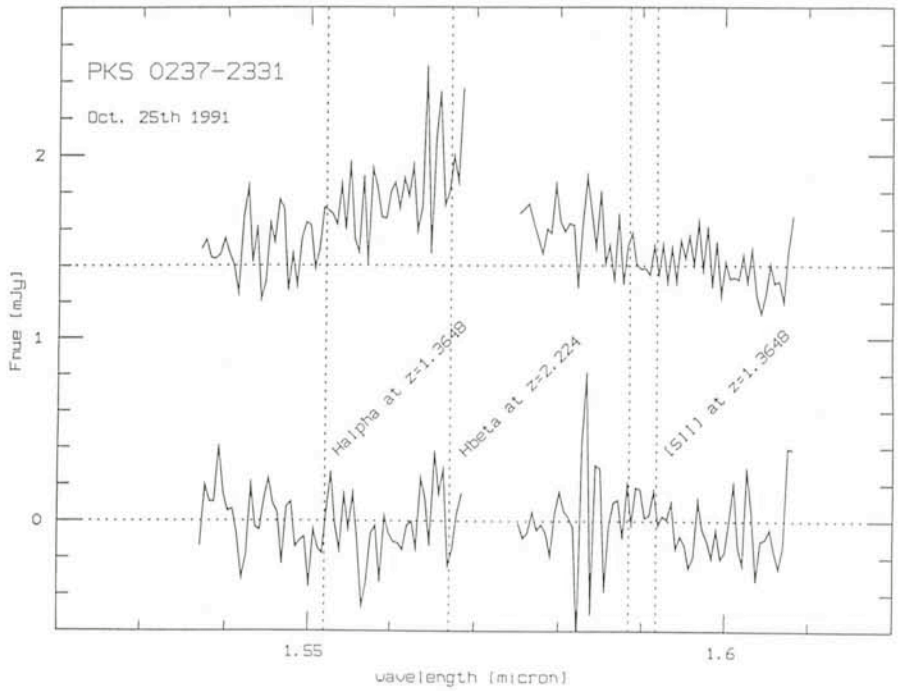

Figure 9: *Spectrum of Hβ at a redshift of z = 2.224 towards the quasar PKS 0237-23 (upper spectrum) and a reference sky position (lower spectrum). The horizontal dotted line in the upper spectrum marks the quasar continuum. The vertical lines show the location of Hα and [SII] at z = 1.3648. The centre of the Hβ line at z = 2.224 is indicated.*

region. Because the redshifts are, in general, larger than one, many of these transitions are shifted into the infrared domain. Figure 9 contains the spectrum between 1.54 μm and 1.61 μm towards the quasar PKS 0237-23 (Käufl et al. 1992) which has a redshift of z = 2.224. The lower part contains the spectrum of a reference position for comparison. The observations were aimed to detect Hα in emission and the [SII] doublet at z = 1.3648, which corresponds to the redshift of previously reported UV absorption lines. The total integration time is 16,000 s. Hα emission is not seen at z = 1.3648. The upper limit in the Hα luminosity of 2.5×10^{42} erg s^{-1} indicates that the star-formation rate in the intervening system is 22–36 $M_\odot$/yr at most. The continuum of the quasar in H is 1.4 ± 0.2 mJy. The Hβ line is detected at the redshift of the quasar, however. The gap in the spectrum right at the peak of Hβ reflects the serendipitous character of the observation. The line width is 4000 km/s and agrees with that of Hα, earlier detected in PKS 0237-23.

Acknowledgements

It is a pleasure to thank H.U. Käufl, A. Moorwood, E. Oliva, and L. Origlia for providing some of their unpublished results, and E. Oliva for making available his MIDAS routines to correct for the spectral line tilt.

References

Gredel, R., Reipurth, B., and Heathcote, S.: 1992, *A&A*, in press.

Käufl, H.U., Rosa, M., Caulet, A., and Viegas, S.M.: 1992, submitted to *A&A*.

Moorwood, A.F.M., and Oliva, E.: 1992, to appear in *PASP Proceedings of Calgary Infrared Spectroscopy Conference*.

Moorwood, A.F.M. and Oliva, E.: 1992, in preparation.

Origlia, L., Oliva, E., and Moorwood, A.F.M. 1992, *A&A*, submitted.

Reipurth, B. 1991, *Nature* **340**, 42.

TIMMI at the 3.6-m Telescope

H. U. KÄUFL, ESO

R. JOUAN, P. O. LAGAGE, P. MASSE, P. MESTREAU, A. TARRIUS, DAPNIA/SAP, CEN-Saclay, France

Careful readers of *The Messenger* may have stumbled over the acronym TIMMI occurring in the context of instrumentation in various previous issues (see e.g. No. **61**, p. 58). In this article we report about the first commissioning run on La Silla in July 1992 and give a short description of the instrument. TIMMI stands for Thermal Infrared Multimode Instrument. TIMMI is supposed to become a general user instrument allowing for imaging as well as limited long-slit spectroscopy in the 10-μm atmospheric window. The project started in July 1990 when ESO signed a contract with the Service d'Astrophysique of the Commissariat à l'Energie Atomique for the development and supply of TIMMI (Principal Investigator: P.O. Lagage). The instrument was then built by the SAP according to ESO's specification in a period of two years.

1. Description of TIMMI

Like all infrared instrumentation TIMMI is a cryogenic instrument. It is mounted inside a Solid Nitrogen/Liquid Helium cryostat. Its optical principle is best described as an "infrared EFOSC". The optics consists of a f=136-mm lens having a triple function: entrance window to the Dewar, focal reduction and field lensing. The telescope focal plane is located inside of the Dewar. Behind a f=103-mm collimator there is a 3.6-mm ∅ pupil stop. The filterwheel is located behind that pupil stop in the collimated beam. This is followed by a lens-wheel.

The camera has three mechanical functions (operated remotely under computer control): a mechanism to exchange the cryogenic field mask with a cryogenic slit assembly, a filterwheel and a lenswheel. Figure 1 shows the non-trivial parts of the camera disassembled. The camera is interfaced to the telescope with the standard infrared adaptor (see Fig. 2) and utilizes the f/35 chopping secondary unit. It can be mounted both at the 3.6- and 2.2-m telescopes. At present, however, operation is foreseen primarily at the 3.6-m telescope.